# Improvements in the accuracy and statistical variance of the Monte Carlo simulation of light distribution in tissue

Gardner, Craig, Welch, Ashley

Craig M. Gardner, Ashley J. Welch, "Improvements in the accuracy and statistical variance of the Monte Carlo simulation of light distribution in tissue," Proc. SPIE 1646, Laser-Tissue Interaction III, (7 August 1992); doi: 10.1117/12.137485

SPIE.

Event: OE/LASE '92, 1992, Los Angeles, CA, United States

# Improvements in the accuracy and statistical variance of the Monte Carlo simulation of light distribution in tissue

Craig M. Gardner, Ashley J. Welch

Biomedical Engineering Program, University of Texas at Austin
Austin, TX 78712

## ABSTRACT

Monte Carlo simulations provide accurate descriptions of light distribution in complex geometry, multiple layer tissues at the expense of long computation times. In addition, the accuracy of the light distribution quantity calculated is influenced by the resolution of the simulation if spatial convolution is used. A method of increasing the accuracy of the calculated fluence rate without increasing computation time is to consider the Beer-Lambert law source attenuation in the tissue analytically, separate from the Monte Carlo numeric calculation of the remaining multiple scattering process. A method of reducing the time of computation needed for a desired maximum statistical variance is to use a non-linear grid that provides high resolution in areas of interest and lower resolution far away from the source and boundaries. The theory of the source attenuation function is discussed. Results demonstrating the validity of the analytic function and the use of non-linear grids are provided and compared to standard Monte Carlo techniques.

## 1. INTRODUCTION

Monte Carlo methods have been used to model light distributions in biological tissue for the past nine years. Wilson and Adam [1] first adopted Monte Carlo techniques to visible electromagnetic radiation from studies of x-radiation in tissue. Since then Monte Carlo simulations have used a number of algorithms [2, 3, 4, 5] to calculate both static [6, 7, 8, 9] and dynamic [10, 11, 12] radiative quantities.

Monte Carlo simulations of light distribution are based on the probabilistic nature of the interaction between a medium and electromagnetic radiation. Specifically, light is treated as non-interacting photon bundles, and tissue is stochastically identified by probability density functions for light attenuation, F(s), and direction of light scatter, $G(\phi)$ and $H(\theta)$ [7]:

$$F(s) = \mu_t e^{-\mu_t s} \tag{1}$$

$$G(\phi) = 1/2\pi \tag{2}$$

$$H(\theta) = (1 - g^2)/[2(1 + g^2 - 2g\cos\theta)^{3/2}] \tag{3}$$

In equation (1), s is the photon bundle pathlength between attenuation events, and $\mu_t$ is the total attenuation coefficient. In equations (2) and (3), $\phi$ and $\theta$ identify the new direction of the scattered photon in a spherical geometry assuming a Henyey-Greenstein single scattering function, where g is the average cosine of the scattering angle. A random number is used to determine the probability of an event (F, G, or H) occurring, and the probabilistic parameter (s, $\phi$, or $\theta$) is calculated. The photon bundle is propagated through the tissue by absorbing a fraction $\mu_a/\mu_t$ of its "weight" after the bundle has travelled the pathlength s, where $\mu_a$ is the tissue absorption coefficient. The remaining weight is scattered in the new direction specified by $\phi$ and $\theta$, measured from the previous photon direction. Refractive index mismatch boundary conditions are handled by calculation of

 0-8194-0792-5/92/$4.00

the Fresnel reflection coefficients, assuming unpolarized light. A complete description of the Monte Carlo method used may be found in [2].

The results of a Monte Carlo simulation are stored as a discrete data array, with an array element representing the number of absorption events that occurred in a volume element at a location in the tissue. If this absorption grid is in cylindrical coordinates, the volume elements are rings centered on the optical axis with volume $2\pi r\Delta r\Delta z$, where r is the radial distance to the ring (see figure 1). If light enters the tissue at the origin (r=0, z=0) and the the number of events in a grid location is normalized by the total number of events occurring in the tissue and the element volume, then the data array represents the discrete, or sampled, point spread function of the tissue.

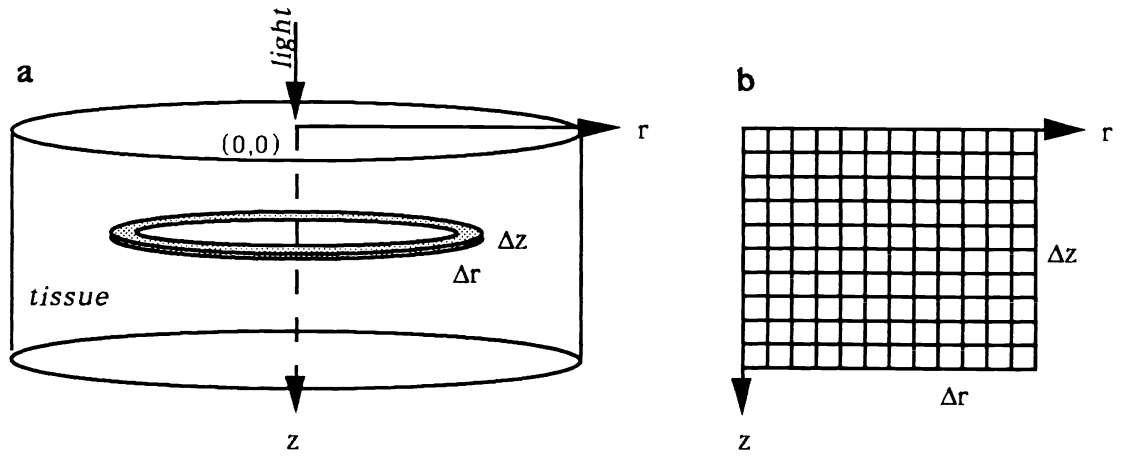


**FIGURE 1.** **a)** Cylindrical coordinate geometry used in Monte Carlo simulations for slab geometry. Light enters the tissue at (0,0). **b)** Corresponding array used to generate point spread function.

For cylindrical coordinate geometry the first volume element is centered radially at $\Delta r/2$, and therefore approximately represents the point spread function at ($r=\Delta r/2$, z). However, first absorption events of photon bundles injected into the tissue at (r=0, z=0) occur on axis, but are recorded as occurring at $\Delta r/2$. Therefore an error in the final calculated result will occur near the light source. An analytic function representing Beer's Law attenuation of the light source may be introduced to accurately record on-axis absorption events. Section 2 describes the theory behind this analytic function.

The time of computation needed for Monte Carlo simulations to achieve an accuracy better than analytical methods such as the diffusion approximation to the radiative transport equation is a concern to some researchers. The trade-off in decreasing simulation time is a decrease in the spatial resolution of the result. Ideally, each volume element should be as large as possible to collect photon absorption events more rapidly and to achieve acceptable statistical variance in less time. Furthermore, high resolution is needed only in certain areas of the tissue geometry such as near the source and near boundaries between different tissues. In other areas the fluence rate changes more gradually, and lower spatial resolution is sufficient. The use of a spatially non-linear absorption grid may decrease computation times while not sacrificing spatial resolution. Simulations using non-linear absorption grids are described in section 3.

## 2. THEORY

### 2.1. Continuous point spread function

For a semi-infinite, slab geometry tissue, the point spread function in cylindrical coordinates may be written as

$$G(r,z) = G_c(z)\delta(r) + G_s(r,z) \tag{4}$$

where $G_c(r,z)$ is the absorption pattern of the first absorption events along (r=0,z) and $G_d(r,z)$ is the continuous point spread function of scattered photons injected at (r=0, z=0). The function describing first absorption events is

$$G_c(r,z) = \mu_a e^{-\mu_t z} \tag{5}$$

The total rate of heat generation for a circular symmetric irradiance pattern E(r) is the convolution (*) of the point spread function and the irradiance pattern:

$$S(r,z) = G(r,z) * E(r) \tag{6a}$$

$$= G_c(z)\delta(r) * E(r) + G_d(r,z) * E(r) \tag{6b}$$

$$= \mu_a e^{-\mu_t z} E(r) + G_d(r,z) * E(r) \tag{6c}$$

The corresponding fluence rate is the rate of heat generation divided by the absorption coefficient:

$$\Phi(r,z) = e^{-\mu_t z} + G_d(r,z) * E(r) \tag{7}$$

### 2.2. Discrete point spread function

The discrete point spread function for the geometry of figure 1 is

$$G(r,z) = \frac{1}{2\pi\Delta z}\left[\frac{1}{r\Delta r}c(z)\delta(r) + \frac{1}{r\Delta r}F_d(r,z)\right] \tag{8}$$

where the first additive term on the left side is the contribution of the first absorption events, and the second term is the contribution from all scattered photon absorption events. The term c(z) represents the fraction of first event photons absorbed over an interval $\Delta z$ due to Beer's law attenuation with axial distance:

$$c(z) = \left[e^{-\mu_t(z - \Delta z/2)} - e^{-\mu_t(z + \Delta z/2)}\right]\left[\frac{\mu_a}{\mu_t}\right] \tag{9}$$

The fluence rate, $\Phi(r,z)$, for a source with collimated irradiance normally incident on the tissue surface, E(r), is the convolution of the point spread function and the source irradiance in cylindrical coordinates [2]:

$$\Phi(r,z) = \frac{1}{\mu_a}\int_0^\infty G(r',z)\int_0^{2\pi} E\left(\sqrt{r^2 + r'^2 - 2rr'\cos\theta}\right) d\theta\, r'\, dr' \tag{10}$$

When this integral is calculated numerically using the discrete point spread function from (8), the $1/r\Delta r$ terms cancel with the integration step size and the calculated fluence rate is

$$\Phi_{SAF}(r,z) = \frac{c(z)}{\Delta z \mu_a} E(r) + \Phi_d(r,z) \tag{11}$$

where $\Phi_d(r,z)$ is the fluence rate due to scattered light. Equation (11) may be rewritten using equation (9) as

$$\Phi_{SAF}(r,z) = \frac{-1}{\mu_t}\left[\frac{e^{-\mu_t(z+\Delta z/2)} - e^{-\mu_t(z-\Delta z/2)}}{\Delta z}\right] E(r) + \Phi_d(r,z) \tag{12}$$

Note that when the limit of equation (12) as $\Delta z \to 0$ is taken, the fluence rate is

$$\Phi_{SAF}(r,z) = \frac{-1}{\mu_t}\frac{d}{dz}\left[e^{-\mu_t z}\right] S(r) + \Phi_d(r,z) \tag{13a}$$

$$= e^{-\mu_t z} S(r) + \Phi_d(r,z) \tag{13b}$$

The first term is therefore the collimated source irradiance attenuated exponentially according to Beer's Law along its direction of travel.

Typically in Monte Carlo simulations the recording of first absorption events are displaced to the first volume element of the sampled function. In this case, the point spread function and fluence rate are

$$G_{dis}(r,z) = \frac{1}{2\pi\Delta z}\left[\frac{1}{r\Delta r} c(z)\delta(r - \Delta r/2) + \frac{1}{r\Delta r} F_d(r,z)\right] \tag{14}$$

$$\Phi_{dis}(r,z) = \frac{c(z)}{\Delta z \mu_a} \Theta(r, \Delta r/2) + \Phi_d(r,z) \tag{15}$$

where

$$\Theta(r,\Delta r/2) = \frac{1}{2\pi}\int_0^{2\pi} E\left(\sqrt{r^2 + (\Delta r/2)^2 - 2r(\Delta r/2)\cos\theta}\right) d\theta \tag{16}$$

The error in displacing first absorption events to $r=\Delta r/2$ may be defined as the difference of equations (15) and (11). If this difference is normalized to the peak irradiance of the source, the error is:

$$\varepsilon(r,z) \equiv \frac{1}{E_o}\left[\Phi_{dis}(r,z) - \Phi_{SAF}(r,z)\right] \tag{17}$$

For a gaussian source with peak irradiance $E_o$ and $1/e^2$ beam radius $\omega_o$, the error may be written using equation (9), (11), (15), and (16) as

$$\varepsilon(r,z) = \left\{ \frac{e^{-\mu_t z} \sinh(\mu_t \Delta z/2)}{\mu_t \Delta z/2} \right\} \left\{ e^{-2(r/\omega_o)^2} \left[ I_o\left(2r\Delta r/\omega_o^2\right) e^{-(\Delta r/\omega_o)^2/2} - 1 \right] \right\} \quad (18a)$$

$$= \varepsilon_z(\mu_t z, \mu_t \Delta z)\, \varepsilon_r(r/\omega_o, \Delta r/\omega_o) \quad (18b)$$

where $I_0(x)$ is the zero-order modified Bessel function. Note that the error in locating first absorption events at $\Delta r/2$ for gaussian beams may be grouped into two terms, one with axial parameters only and the other with radial parameters only.

## 3. SIMULATIONS

### 3.1. Linear grid simulations

Monte Carlo simulations were performed for a range of absorption and scatter coefficients listed in table 1, a constant average cosine of scattering angle of 0.8, and a constant refractive index mismatch of air/tissue equal to 1.0/1.4. The attenuation coefficient, transport albedo and diffusion approximation penetration depth are defined and calculated for each combination in table 1.

The resolution of the sampled point spread function was such that the volume element radius and thickness were $\Delta r = \Delta z = 1$ mm. The size of the sampled point spread functions was made such that the last radial element was a distance of 15 mm or 12 penetration depths from the optical axis, whichever quantity was smaller. This ensures that the convolution will accurately estimate the fluence rates by including appreciable contribution to the point spread function far from the source [13]. The simulations were run until 100 absorption events were recorded in the last radial ring located between z=0 and $z=\Delta z/2$.

| $\mu_a$ [mm$^{-1}$] | $\mu_s$ [mm$^{-1}$] | $\mu_t$ [mm$^{-1}$] | $a_{tr}$ | $\delta$ [mm] |
|---|---|---|---|---|
| 0.1 | 3.0 | 3.1 | 0.86 | 2.2 |
| 0.1 | 10.0 | 10.1 | 0.95 | 1.3 |
| **0.1** | **30.0** | **30.1** | **0.98** | **0.74** |
| 0.3 | 3.0 | 3.3 | 0.67 | 1.3 |
| 0.3 | 10.0 | 10.3 | 0.87 | 0.70 |
| 0.3 | 30.0 | 30.3 | 0.95 | 0.42 |
| 1.0 | 3.0 | 4.0 | 0.36 | 0.46 |
| 1.0 | 10.0 | 11.0 | 0.67 | 0.33 |
| 1.0 | 30.0 | 31.0 | 0.86 | 0.22 |

**TABLE 1.** Absorption and scatter coefficient simulation parameters. For each $\mu_a/\mu_s$ pair the attenuation coefficient is $\mu_t = \mu_a + \mu_s$, the transport albedo is $a_{tr} = \mu'_s/(\mu_a + \mu'_s)$, the penetration depth is $\delta = 1/(3\mu_a(\mu_a + \mu'_s))^{1/2}$, and $\mu'_s = \mu_s(1\text{-}g)$. The combination printed in bold face was also used in simulation with a non-linear absorption array.

### 3.2. Non-linear grid simulations

A simulation was also run using a spatially non-linear array to sample the point spread function for the absorption and scatter coefficient pair printed in bold face in table 1. The surrounding medium was refractive index matched to the tissue. The non-linear array was made such that the the first K radial and L axial volume elements had sampling widths of $\Delta r_o$ and $\Delta z_o$. The remaining array elements had sampling widths proportional to

their radial and axial distance from the origin. For the element identified by the position $(r_i, z_j)$, the spatial resolution is given by

$$\Delta r_i = \begin{cases} \Delta r_o & i \le K \\ (\Delta r_o / r_K) r_i & i > K \end{cases} \tag{19}$$

$$\Delta z_j = \begin{cases} \Delta z_o & j \le L \\ (\Delta z_o / z_L) z_j & j > L \end{cases} \tag{20}$$

The non-linear grid is depicted in figure 2. The maximum resolution of the non-linear array was such that $\mu_t \Delta r_o = 3$ optical depths and $\mu_t \Delta z_o = 1$ optical depth. The number of linear radial array elements, K, was chosen such that the last radial ring, located at r=3 mm, had a width of $\mu_t \Delta r = 10$ optical depths.

Two linear grid simulations for each tissue parameter pair were also made performed. The first linear grid had resolution corresponding to $\mu_t \Delta r = 3$ optical depths and $\mu_t \Delta z = 1$ optical depths, the same as the maximum resolution of the non-linear grid. The second linear grid had sampling widths of $\mu_t \Delta r = \mu_t \Delta z_o = 10$ optical depths. The linear grids also extended radially to 3 mm.

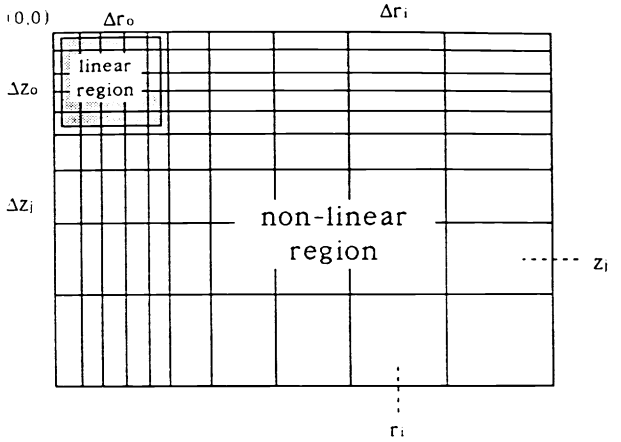


**FIGURE 2.** Spatially non-linear absorption grid. The grid has a linear region near the light source with constant resolution. The remaining grid elements have resolution proportional to their distance from the optical axis.

### 3.3. Convolutions

Fluence rates were calculated for gaussian beams with $1/e^2$ radii of 1, 3, and 5 mm, for each point spread function generated in Monte Carlo simulations. The non-linear simulation was convolved with the 1 mm gaussian beam only. The convolutions were calculated numerically using a series approximation for the zero-order modified Bessel function needed for gaussian source irradiance [2].

The convolution error resulting from locating first absorption events at $\Delta r/2$ was calculated from the same simulation to avoid errors due to statistical variance of the result. Fluence rate calculations for the proper recording of the first absorption events was accomplished using equation (11). First absorption events were included in the discrete convolution of the point spread function with the gaussian beam irradiance for the case of improper location of first absorption events.

## 4. RESULTS AND DISCUSSION

Figure 3 displays the simulated and theoretical error when first absorption events are not recorded on axis for three of the point spread function simulations, each convolved with a different gaussian beam size. The errors are plotted versus radial position for a tissue depth of $z=\Delta z/2$. Negative errors occur near the optical axis, while positive errors occur near the $1/e^2$ beam radius. Note that the simulated errors are the same as the theoretical error calculated from equation (19); therefore, the theory may be used to calculated errors based on dimensionless axial and radial parameters. The error depends only upon the resolution of the point spread function array, the size of the beam, and the total attenuation coefficient of the tissue.

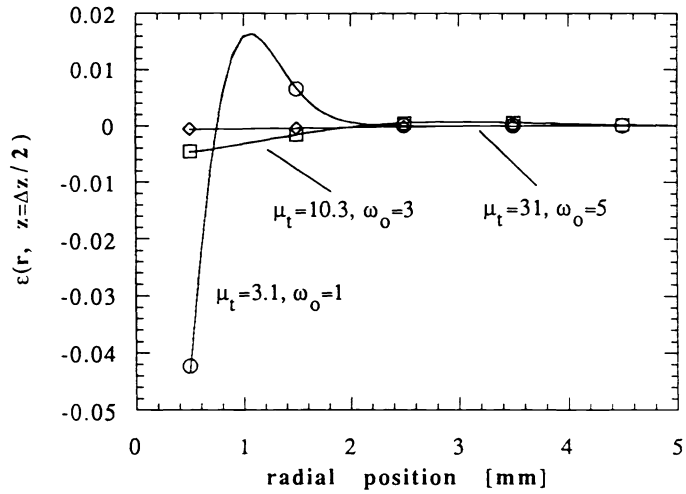


**FIGURE 3.** Comparison of simulated (data points) and theoretical (lines) errors when not using the source attenuation function. The total attenuation coefficient, $\mu_t$ [$mm^{-1}$], and gaussian beam radius, $\omega_o$ [mm], are identified for each set of data. Theoretical errors were calculated using equation (15).

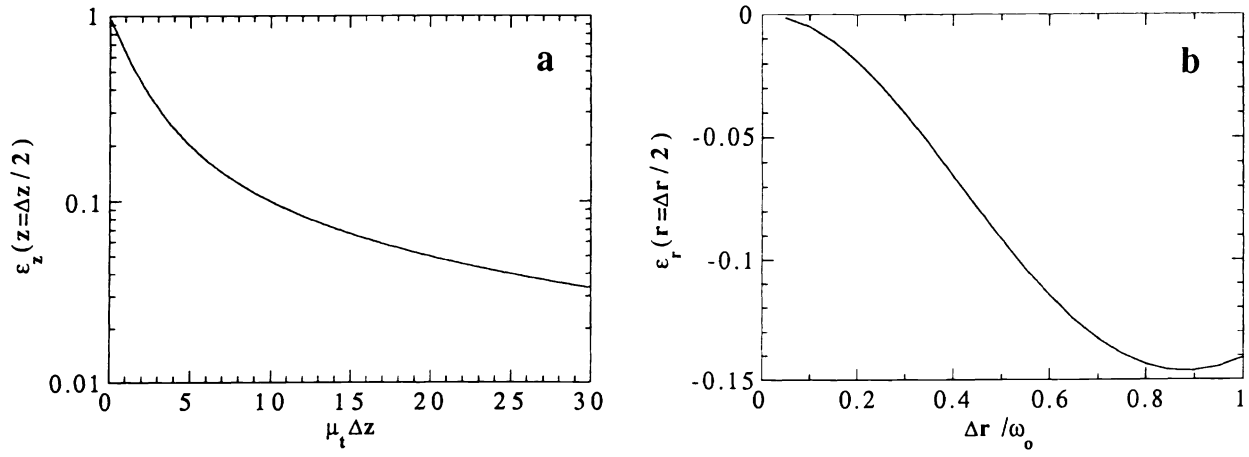


**FIGURE 4.** The maximum error when not using the source attenuation function with a gaussian beam occurs at ($r=\Delta r/2$, $z=\Delta z/2$). **a)** Maximum error contribution from axial terms of equation (18b), plotted versus axial sampling width, $\mu_t\Delta z$ [optical depth]. **b)** Maximum error contribution from radial terms of equation (18b), plotted versus radial sampling width, $\mu_t\Delta r$ [optical depth].

The maximum error in the three-dimensional light distribution pattern is negative and occurs in the volume element closest to the center of the light source, located at ($r=\Delta r/2$, $z=\Delta z/2$). Figure 4 displays this maximum error separated into contributions due to the dimensionless parameters $\mu_t \Delta z$ and $\Delta r/\omega_0$, as in equation (18b). Note that the maximum error increases as $\mu_t \Delta z$ decreases, but also as $\Delta r/\omega_0$ increases. This fact tends to keep the error small for most simulation cases; but note that when the axial resolution is comparable to an optical depth ($1/\mu_t$) and the radial resolution is comparable to the beam radius, the error is near its maximum value. This combination of parameters is not unrealistic. For example, when the goal of the simulation is to determine the rate of heat generation just below the tissue surface, $\Delta z$ should be small to resolve subsurface fluence rate maxima, whereas $\Delta r$ need only be comparable to the beam size.

Inclusion of the correct recording of Beer's law attenuation into Monte Carlo algorithms is straightforward. The first absorption events of photon bundles should be stored in a one-dimensional absorption array identifying absorption at the tissue locations ($r=0$, $z$), and therefore should not be included in the two-dimensional array used for the scattered bundle absorption events. This array may then be added to the calculation of the fluence rate after the discrete convolution involving the scattered photon events, according to equation (11).

The error in displacing first absorption events to the first array elements depends on the coordinate geometry used because of the different forms of convolution needed. Cartesian and spherical coordinate geometries will therefore have different theoretical equations describing the error. Unpublished preliminary calculations show that larger errors will occur when Cartesian geometry is used for convolution instead of cylindrical coordinate geometry. The error will also vary with the shape of the source irradiance. For example, a circular beam with uniform irradiance will have errors only near the edge of the beam.

Figure 5 compares axial fluence rates for simulations using the linear grid with a 10 optical depth sampling rate, and the non-linear grid. Also listed are the computation time used for each simulation. Although the time of simulation for the linear grid is appealing, the result does not display the complexity of the light distribution pattern. If constructed properly, a non-linear grid is more time efficient than a linear grid of comparable resolution. For the linear and non-linear simulations with identical maximum resolution, the non-linear simulation was 45% faster. The comparative efficiency of the non-linear grid will vary with exact non-linear form and parameters used.

The advantage of using a non-linear grid is that the resolution may be matched to the shape of the point spread function. Figure 6 displays how rapidly the point spread function for highly scattering tissues decreases with radial distance near the light source. Just as the resolution of the grid should be made small enough to resolve the profile of the incident light source, the grid should also resolve the point spread function at all locations in the tissue. The figure demonstrates that the point spread function, not including first absorption events, is resolved when the radial sampling width is 3 optical depths. In general, sampling widths near the source should be made on the order of 1 optical depth, over a distance of 5 to 10 optical depths, to resolve the point spread function. Radial sampling widths farther away may be made comparable to the smallest beam size for which the fluence rate is needed.

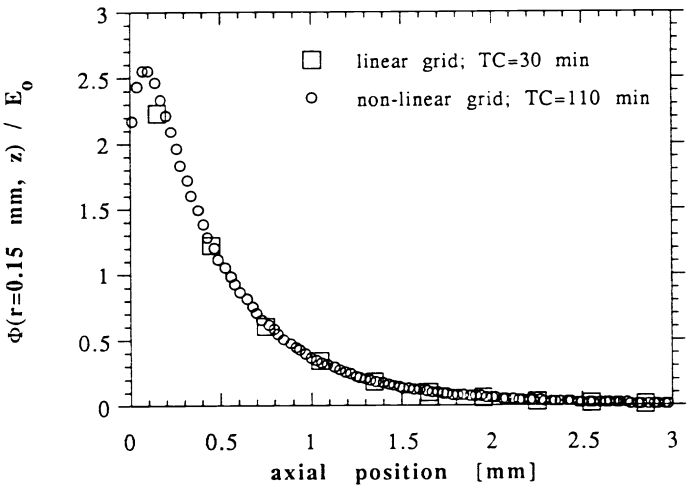


**FIGURE 5.** Comparison of normalized axial fluence rates for a 1 mm radius gaussian beam, $\Phi(r,z)/E_o$, computed from linear and non-linear point spread function grids. The axial sampling widths of the linear and non-linear grids are $\mu_t\Delta z=10$ and 1 optical depths, respectively. Both fluence rates are displayed for a radial position of r=0.15 mm. The legend lists the computation time (CT) for the two simulations. The total attenuation coefficient is 30.1, and the transport albedo is 0.98.

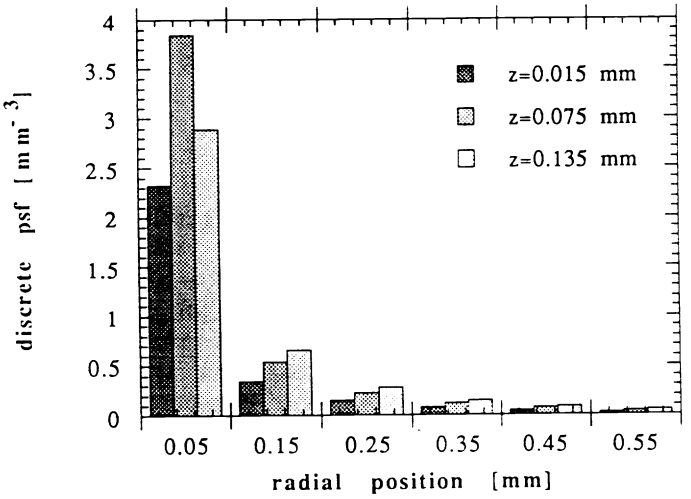


**FIGURE 6.** Point spread function without first absorption events, plotted radial position for tissue depths of z=0.015 mm, 0.075 mm, and 0.135 mm. The total attenuation coefficient is 30.1, and the transport albedo is 0.98.

## 5. CONCLUSIONS

Non-linear absorption grids used in Monte Carlo simulations may be used effectively to resolve the point spread function of the tissue as well as the source irradiance. In addition, the use of non-linear grids may decrease the computation time needed to achieve acceptable statistical variance compared to linear grids.

Errors in the accuracy of fluence rate may occur due to improper recording of the Beer's law attenuation of the point spread function source. When cylindrical coordinate geometry is used to calculate the point spread function and to perform the convolution with

a gaussian beam, the maximum error occurs in the volume element closest to the surface and optical axis. This error leads to an underestimate of the actual fluence rate by no more than 15%. An overestimation of the fluence rate occurs near the $1/e^2$ radius of the beam.

The form of this error varies with the coordinate geometry used and method of convolution. A theoretical error may be easily derived for cartesian coordinate geometry in the same manor. In either case, the implementation of an analytic source attenuation function into Monte Carlo simulations is straight forward and will improve the accuracy of any calculated radiative spatial quantity.

## 6. ACKNOWLEDGMENTS

We thank Dr. Steve Jacques for his thoughts on the convolution error, and Danielle Beaucamp for initiating discussion of the accuracy of convolution. This work was supported in part by the Office of Naval Research under grant N00014-91-J-1564 and the Albert and Clemmie Caster Foundation.

## 7. REFERENCES

[1] Wilson B.C. and Adam G., "A Monte Carlo model for the absorption and flux distribution of light in tissue," *Med Phys* **10**: 824-830; 1983.

[2] Prahl S.A., "Light propagation in tissue," Doctoral dissertation, University of Texas at Austin; 1988

[3] Bonner R.F., *et al.* "Model for photon migration in turbid biological media," *J Opt Soc Am A* **4**: 423-433; 1987.

[4] Wyman D.R., *et al.*, "Similarity relations for anisotropic scattering in Monte Carlo simulations of deeply penetrating neutral particles," *J Comp Phys* **81**: 137-150; 1989.

[5] Flock S.T., *et al.*, "Hybrid Monte Carlo-Diffusion theory modeling of light distribution in tissue," in *SPIE* **908**: 20-28; 1988.

[6] Flock S.T., *et al.*, "Monte Carlo modeling of light propagation in highly scattering tissues-II: Comparison with measurements in phantoms," *IEEE Trans Biomed Eng* **36**: 1169-1173; 1989.

[7] Keijzer M., *et al.*, "Light distribution in artery tissue: Monte Carlo simulation for finite-diameter beams," *Lasers Surg Med* **9**: 148-154; 1989.

[8] Jacques S.J. and Keijzer M., "Dosimetry for lasers and light in dermatology: Monte Carlo simulations of 577 nm pulsed laser penetration into cutaneous vessels," *SPIE* **1422**: 2-13 ;1991.

[9] Welch A.J. and Gardner C.M., "Monte Carlo model for the determination of the rate of heat generation in laser irradiated tissue," *Proc International Symposium on Heat and Mass Transfer in Biomedical Engineering*; in press.

[10] Jacques S.J., "Time resolved reflectance spectroscopy in turbid tissues," *IEEE Trans Biomed Eng* **36**: 1155-1161; 1989.

[11] Haselgrove J.C., *et al.*, "Monte Carlo and diffusion calculations of photon migration in noninfinite highly scattering media," *SPIE* **1431**: 30-41; 1991.

[12] Yamada Y. and Hasegawa Y., "Simulation of time-resolved optical-CT imaging," *SPIE* **1431**: 73-82; 1991.

[13] Jacques S.J. and Wilson B.C., "Optical reflectance and transmittance of tissues: principles and applications," *IEEE J Quant Elec* **26**: 2186-2199; 1990.